

Nodeless superconductivity in the type-II Dirac semimetal PdTe₂: London penetration depth and pairing-symmetry analysis

S. Teknowijoyo,^{1,2} Na Hyun Jo,^{1,2} Mathias S. Scheurer,³ M. A. Tanatar,^{1,2} Kyuil Cho,¹ S. L. Bud'ko,^{1,2} Peter P. Orth,² P. C. Canfield,^{1,2} and R. Prozorov^{1,2,*}

¹*Division of Material Science and Engineering, Ames Laboratory, Ames, Iowa 50011, USA*

²*Department of Physics and Astronomy, Iowa State University, Ames, Iowa 50011, USA*

³*Department of Physics, Harvard University, Cambridge, Massachusetts 02138, USA*



(Received 2 April 2018; revised manuscript received 18 June 2018; published 16 July 2018)

Superconducting gap structure was probed in type-II Dirac semimetal PdTe₂ by measuring the London penetration depth using the tunnel diode resonator technique. At low temperatures, the data for two samples are well described by a weak-coupling exponential fit yielding $\lambda(T = 0) = 230$ nm as the only fit parameter at a fixed $\Delta(0)/T_c \approx 1.76$, and the calculated superfluid density is consistent with a fully gapped superconducting state characterized by a single gap scale. Electrical resistivity measurements for in-plane and inter-plane current directions find very low and nearly temperature-independent normal-state anisotropy. The temperature dependence of resistivity is typical for conventional phonon scattering in metals. We compare these experimental results with expectations from a detailed theoretical symmetry analysis and reduce the number of possible superconducting pairing states in PdTe₂ to only three nodeless candidates: a regular, topologically trivial *s*-wave pairing, and two distinct odd-parity triplet states that both can be topologically nontrivial depending on the microscopic interactions driving the superconducting instability.

DOI: [10.1103/PhysRevB.98.024508](https://doi.org/10.1103/PhysRevB.98.024508)

I. INTRODUCTION

Finding materials that exhibit topological superconductivity is one of the primary goals of current research efforts in condensed matter physics, mainly motivated by their unique Majorana surface state properties [1–3]. These protected non-Abelian surface modes [4,5] can, for example, be exploited in quantum computing schemes [6]. The search for topological superconductors (TSCs) has recently been boosted by the discovery of various material classes that feature topological band structures already in the normal state. There are multiple scenarios in which superconducting pairing among such states, characterized by a nonzero topological invariant [e.g., a (mirror) Chern number], are (at least theoretically) known to result in the emergence of topological superconductivity [1–3].

There are several examples of such a scenario. For instance, superconductivity arises in topological insulators either from doping such as in Cu_xBi₂Se₃ [7–9] and Sb₂Te₃ [10], or from proximity coupling of the 2D Dirac surface state to a regular *s*-wave SC [2,11]. Other examples are semiconductor heterostructures and 1D quantum wires with strong spin-orbit coupling and (proximity-induced) superconductivity [12]. Further candidate systems are magnetic, i.e., inversion-symmetric (but time-reversal-symmetry breaking), Weyl semimetals (SMs) that are predicted to favor odd-parity (often topological) pairing over ordinary even-parity pairing [3,13,14]. This is a result of the unique spin texture on the Fermi surfaces surrounding the Weyl points [3,15]. In addition,

time-reversal-invariant (but noncentrosymmetric) Weyl SMs were theoretically shown to host topological superconductivity for suitable electronic interactions [16]. Three-dimensional Dirac SMs such as Cd₂As₃ [17], Na₃Bi [18] (type-I), and PdTe₂ [19] (type-II) are proper starting points to realize Weyl SMs by either breaking inversion or time-reversal symmetry, e.g., via magnetic order or external fields. Moreover, Dirac SMs have been predicted to be a rich platform for topological crystalline SCs with Majorana surface modes arising from a nonzero mirror Chern number. Such a scenario requires the presence of a mirror symmetry, and was proposed to occur in the *C*₄ symmetric systems Cd₂As₃ and Au₂Pb [3,20].

Here, we investigate superconductivity in single crystals of the transition metal dichalcogenide PdTe₂ (space group *P* $\bar{3}m1$), which is a type-II Dirac SM [19,21–23]. As shown by ARPES and band structure calculations [21,22], the Dirac band crossing occurs about 0.6 eV below the Fermi energy and is protected by *C*₃ rotation symmetry. In addition, quantum oscillation measurements of the de Haas–van Alphen effect [21] revealed a nonzero Berry phase in one of the (hole) Fermi surface pockets, confirming the topological nature of the band crossing. Notably, the superconducting state that we study emerges below 1.7 K [24,25].

We report experimental results of the London penetration depth using a tunnel diode resonator (TDR) technique [26]. Our findings clearly indicate a fully gapped superconducting state, in agreement with previous thermodynamic [27], scanning tunnel microscopy (STM) [28], and heat capacity [29] measurements. Combining these experimental insights with a detailed theoretical symmetry analysis, we are able to reduce the possible superconducting pairing states in PdTe₂ to only three candidates, two of which can be topologically nontrivial.

*Corresponding author: prozorov@ameslab.gov

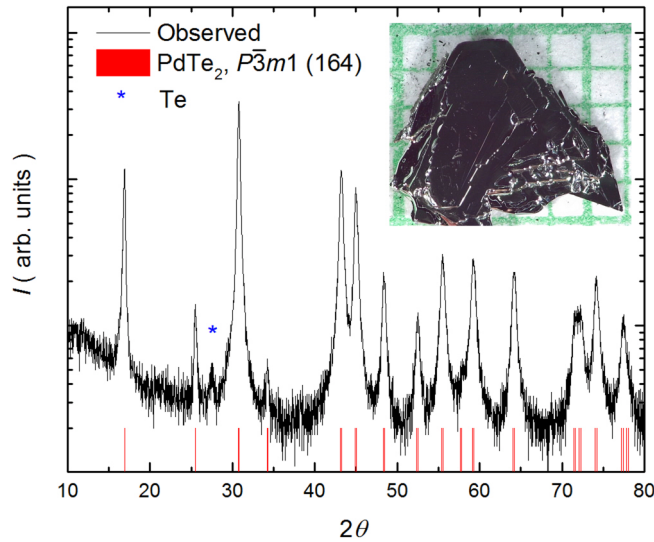


FIG. 1. Powder x-ray diffraction (XRD) pattern of crushed single crystal of PdTe₂ (black line). The red lines are calculated XRD peaks for PdTe₂ with hexagonal structure [$P\bar{3}m1$, 164]. Blue stars mark peaks of solidified Te flux.

The three possible SC pairing states are the standard s -wave BCS state, which is topologically trivial, and two time-reversal-symmetric odd-parity triplet states transforming under the representations A_{1u} and E_u of the point group D_{3d} of the normal state. Whether these odd-parity states are topologically trivial or nontrivial depends on the relative sign of the superconducting order parameter on the two Fermi surfaces [30] enclosing the Γ point in the Brillouin zone and, hence, is determined by whether the electron-electron interactions between the different pockets is repulsive or attractive.

II. EXPERIMENTAL DETAILS

Single crystals of PdTe₂ were grown out of Te-rich binary melts. Elemental Pd (99.9+%) and Te (Alfa Aesar, 99.999+%) were put into a Canfield crucible set (CCS) [31] with initial stoichiometry, Pd_{0.10}Te_{0.90}, and sealed in an amorphous silica tube. The ampules were heated up to 900 °C, within 10 hours, held for 5 hours, cooled to 500 °C, over 120 hours, and finally decanted using a centrifuge [32]. The obtained single crystals of PdTe₂ were hexagonal plate in morphology as shown in the Fig. 1 inset.

A Rigaku MiniFlex II diffractometer (Cu $K\alpha$ radiation with monochromator) was used for acquiring a powder x-ray diffraction (XRD) pattern at room temperature. The acquired patterns are well matched with calculated peaks for hexagonal structure of PdTe₂ with $P\bar{3}m1$ (164) as shown in Fig. 1. The low-intensity extra peak marked with a blue star is associated with residual Te solvent left on the crystals. However, the relative intensity of the peaks is different from the calculated powder pattern, presumably because of the preferential orientation of the ground powder due to the layered structure.

Samples used for four-probe in-plane electrical resistivity, ρ_{\parallel} , measurements were cleaved from inner parts of large single crystals and had dimensions of typically $(2-3) \times 0.5 \times 0.1$ mm³ with the longer side along an arbitrary direction

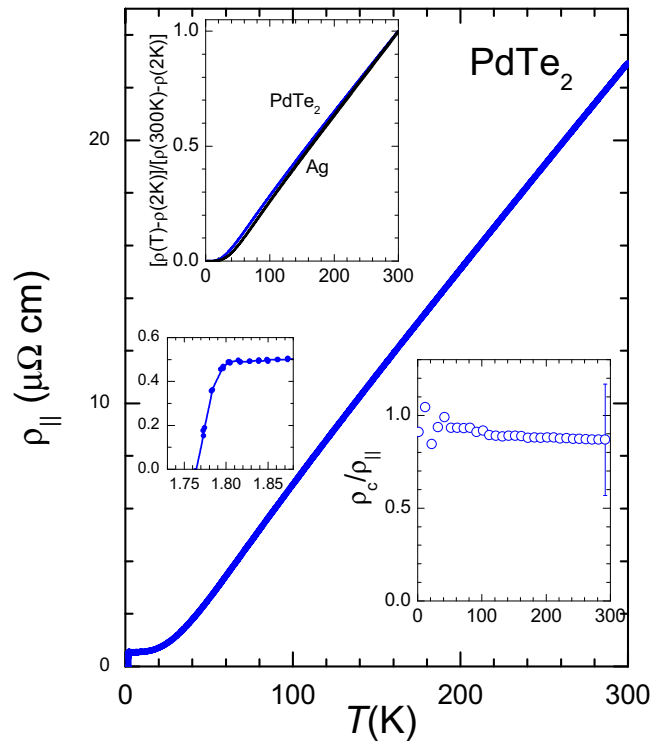


FIG. 2. Temperature-dependent in-plane electrical resistivity of PdTe₂, with bottom left panel showing zoom of the superconducting transition. Note a range below approximately 10 K, where resistivity becomes temperature-independent, and linear increase above 40 K. Left top inset compares normalized temperature-dependent part of resistivity in PdTe₂ and Ag wire [38]. Right inset shows temperature-dependent resistivity anisotropy ratio, ρ_c/ρ_{\parallel} , with error bars determined by uncertainty of experimental geometry.

in the hexagonal plane. Silver wires were soldered using In to the fresh-cleaved surface of the samples [33] to make electrical contacts with sub-m Ω resistance. Sample resistivity at room temperature, as determined on array of 7 samples was $\rho(300 \text{ K}) = 24 \pm 5 \mu\Omega \text{ cm}$. This is consistent with early reports [25] but is notably lower than the $70 \mu\Omega \text{ cm}$ reported recently [29]. Montgomery technique [34,35] measurements were performed on a sample with 1 mm by 0.5 mm cross-section area in the ac plane of the crystal. Contacts were soldered on sample corners covering the whole length of the sample in the third dimension. The large uncertainty of the geometric factor in the crystal due to non-negligible contact size (typically 0.1 mm) compared to the sample size makes these measurements semiquantitative. The anisotropy value $\rho_c/\rho_{\parallel} = 0.9 \pm 0.3$ was found to be temperature independent; see Fig. 2. Temperature-dependent electrical resistivity measurements in four-probe and Montgomery configurations were performed down to 1.8 K in a Quantum Design PPMS. Measurements of the superconducting transition temperature range, below the PPMS range down to 1.8 K, were performed in a cryogen-free He3 system using the same samples and an LS370 resistance bridge from Lake Shore.

Precision in-plane London penetration depth $\Delta\lambda(T)$ measurements using the TDR technique [26] were performed in a high-stability ³He cryostat with a base temperature of

~ 0.4 K. Two samples A and B were measured. The samples were placed with their c axis parallel to an excitation field, $H_{ac} \sim 20$ mOe, much smaller than H_{c1} [27]. The shift of the resonant frequency, $\Delta f(T) = -G4\pi\chi(T)$, is proportional to the differential magnetic susceptibility $\chi(T)$. The constant $G = f_0 V_s / 2V_c(1 - N)$ depends on the resonant frequency, f_0 , demagnetization factor N , sample volume V_s , and coil volume V_c . To avoid uncertainties associated with parameters needed to calculate G , it was experimentally determined by measuring the full frequency change when the sample is physically pulled out of the coil at low temperature. Magnetic susceptibility, $4\pi\chi$, of arbitrarily shaped samples can be described by the expression (exact for a superconducting slab in parallel field) $4\pi\chi = (\lambda/R) \tanh(R/\lambda) - 1$, where λ is the penetration depth and R is the effective geometry-dependent sample dimension [36]. Physically, R takes into account penetration of the magnetic field from all surfaces, not only the sides. From the calculated R and measured $4\pi\chi$, the London penetration depth and its change, $\Delta\lambda(T)$, can be obtained [36,37].

III. RESULTS

The main panel of Fig. 2 shows the temperature-dependent in-plane resistivity of PdTe₂. Despite relatively high resistivity value $\rho(300\text{ K}) = 24\ \mu\Omega\text{ cm}$, the dependence is very typical of a good metal: it is T -linear for $T \gtrsim 40$ K, and flattens below approximately 10 K in the residual resistivity range before the superconducting transition at $T_c \sim 1.76$ K (bottom left inset in Fig. 2) using offset as a criterion for determination. Note that the resistive transition at T_c is very sharp, with the width of 0.04 K, as expected for a high-quality stoichiometric single crystal without substitutional disorder. Direct comparison of the temperature-dependent part of the resistivity, $[\rho(T) - \rho(0)]/[\rho(300\text{ K}) - \rho(0)]$, with that of Ag wire [38] is made in the left top inset in Fig. 2 and finds a nearly perfect match. The slightly lower end of the T -linear range in PdTe₂ is caused by a slightly lower Debye temperature, $\Theta_D \sim 207$ K [39], as compared with 225 K in Ag. This observation clearly identifies phonon scattering as the main scattering mechanism. Nearly isotropic resistivity without noticeable temperature dependence (right bottom inset in Fig. 2) identifies the material as being three-dimensional, in agreement with band structure calculations [40].

The top left inset in Fig. 3 shows the temperature-dependent penetration depth in PdTe₂, measured over the whole range of superconductivity existence. The superconducting transition with $T_c = 1.75$ K is very sharp, in agreement with resistive measurements (see Fig. 2). The main panel of Fig. 3 shows the low-temperature part of the temperature variation of $\Delta\lambda(T)$ in two single-crystalline samples (A, red, and B, blue) of PdTe₂. The data are shown on a normalized temperature scale T/T_c in a temperature range below $0.5T_c$. In the clean limit, the temperature-dependent London penetration depth is expected to be exponential in full-gap superconductors and is expected to be close to T -linear in superconductors with nodes in the gap. The addition of sufficiently strong disorder pushes the dependence to T^2 for both cases [41]. We use a power-law function $\Delta\lambda(T) = A + BT^n$ to quantify the experimental data for the intermediate cases, when the amount

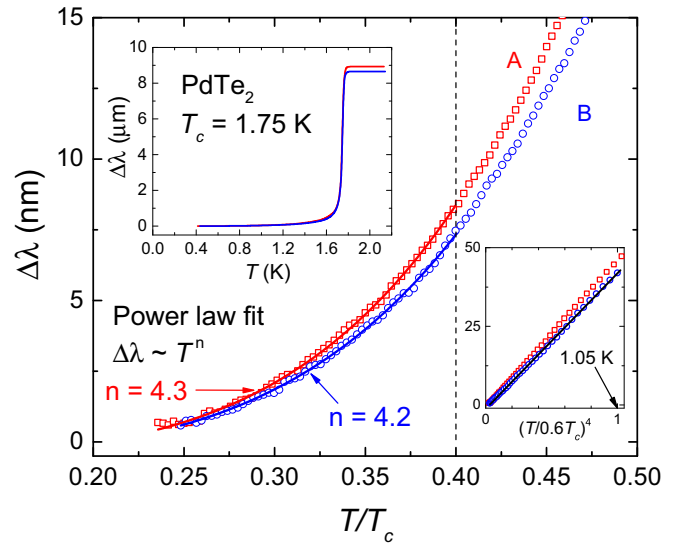


FIG. 3. Temperature variation of London penetration depth $\Delta\lambda(T)$ measured in He³ TDR setup for samples A (red) and B (blue). Main panel shows data with best fit using power-law function $\Delta\lambda(T) = A + BT^n$, with $n = 4.3$ (A) and $n = 4.2$ (B). Right bottom panel shows same data plotted as a function of T^4 to verify quality of the fit. Top inset shows data over the whole temperature range up to $T_c \sim 1.8$ K.

of disorder is not known. Note that the gap magnitude can vary either on the same Fermi surface sheet (gap anisotropy) or between different sheets of the Fermi surface (multiband superconductivity).

It is empirically accepted that a variation described by the power-law function with $n > 3$ corresponds to the case of a full gap, and $n < 2$ corresponds to a nodal case. This fit is made in a characteristic range below $0.3T_c$, in which the temperature dependence of the superconducting gap magnitude is negligible in single-gap superconductors, and the dependence is determined by thermal excitation of quasiparticles across the superconducting gap. The red (blue) line in the main panel of Fig. 3 shows our power-law fit of the data for sample A (B) of PdTe₂ over the range up to $0.4T_c$, which yields the exponent $n = 4.3$ ($n = 4.2$). To check the quality of the fit and justify the extended fitting range up to $0.4T_c$, in the bottom right inset in Fig. 3, we plot the penetration depth data as a function of $(T/T_c)^4$, finding an approximately straight line, verifying $\Delta\lambda \propto (T/T_c)^4$ for a temperature range up to $0.6T_c$ for both samples.

A power-law function with such a large value of the exponent ($n \approx 4$) is indistinguishable from an exponential function (over the range of temperatures observed), which is the expected behavior for penetration depth in a fully gapped BCS superconductor [42]. We therefore also fit our data using an exponential temperature dependence of $\Delta\lambda$. In the top panel of Fig. 4 we show the resulting fit of the London penetration depth data using the regular BCS expression,

$$\Delta\lambda(t \equiv T/T_c) = \lambda(0)\sqrt{\pi\delta/(2t)}e^{-\delta/t} \quad (1)$$

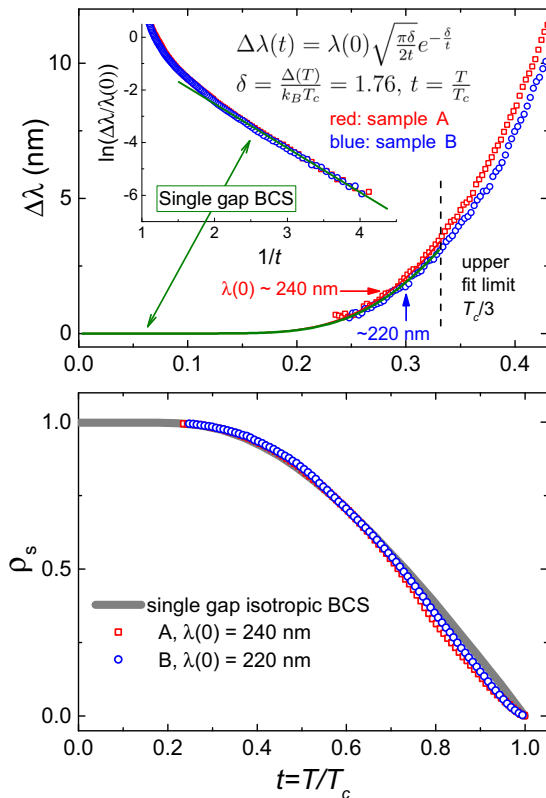


FIG. 4. Top panel: Fit of the temperature variation of London penetration depth with exponential BCS function, enabling determination of $\lambda(0) = 240$ nm (sample A, red) and $\lambda(0) = 220$ nm (sample B, blue). Inset: Logarithmic plot of the BCS function, showing that the function fits the data well in the range $1/t \equiv T_c/T = 2-4$, or $T = 0.25T_c-0.5T_c$. Bottom panel shows calculated superfluid density $\rho_s(T) \equiv [\lambda(0)/\lambda(T)]^2$ using $\lambda(0)$ values extracted from the fit.

with $\delta = \Delta(0)/(k_B T_c) = 1.76$. We obtain a good fit of the penetration depth using the zero-temperature value

$$\lambda(0) = 240 \text{ nm (sample A),} \quad (2)$$

$$\lambda(0) = 220 \text{ nm (sample B).} \quad (3)$$

The determination of $\lambda(0)$ is quite important, since it enters the expression for superfluid density, $\rho_s = \lambda(0)^2/\lambda(T)^2$. The standard tunnel diode resonator technique measures the change in London penetration depth with respect to some starting reference point, usually at the lowest temperature, $\Delta\lambda(T) = \lambda(T) - \lambda(T_{\min})$. However, $\lambda(0)$ can be measured with some additional and quite complicated procedure that involves coating the sample with a thin uniform layer of aluminum [37]. Here for PdTe₂ we can simply use the fact that we can fit the data reasonably well using Eq. (1) valid for a conventional, single-gap, weak-coupling BCS superconductor. The inset in Fig. 4 (top panel) shows that the function matches the data well up to $t = T/T_c = 0.5$. Here $\lambda(0)$ is the only adjustable parameter whereas the gap amplitude is fixed at the weak-coupling ratio, $\Delta_0/k_B T_c = 1.763$. We obtained $\lambda(0) = 230$ nm as the average value for two samples used in this work. This is notably different from the estimate $\lambda(0) = 39$ nm based on Hall effect carrier density [27]. The origin of the

discrepancy may potentially lie in the compensated character of Hall transport in PdTe₂ [21], leading to an overestimate of the carrier density.

Combining our result $\lambda(0) = 230$ nm with a literature value for the coherence length $\xi = 439$ nm taken from Ref. [27], one finds a Ginzburg-Landau parameter $\kappa = \lambda(0)/\xi = 0.52 < 1/\sqrt{2} \approx 0.7$. This is consistent with type-I superconductivity, which was reported previously [27]. Note that the published version of Ref. [27] states $\xi = 114$ nm, which is a typo [43].

The previously determined $\lambda(0)$ allows us to construct the temperature-dependent normalized superfluid density as $\rho_s = [\lambda(0)/\lambda(T)]^2$, with $\lambda(T) = \lambda(0) + \Delta\lambda(T)$. In the bottom panel of Fig. 4 we show the resulting superfluid density ρ_s , calculated using our experimental data and the values $\lambda(0)$ as determined from the exponential fit. The data are plotted versus temperature T/T_c (normalized to T_c), and compared with BCS expectations for a single fully gapped superconductor (thick gray line). The onset $T_c = 1.75$ K is used for both samples, which give curves that lie close to expectations for BCS full-gap superconductors. This clearly shows that superconductivity in PdTe₂ is characterized by a single and full superconducting gap.

IV. DISCUSSION

In the following, we will discuss the implications of our experimental findings for the possible superconducting order parameters. Focusing on superconducting phases that do not break lattice translation symmetry, we can classify different pairing states according to the irreducible representations (IRs) of the point group $D_{3d} = \bar{3}_m^2$ of the normal state of PdTe₂. The resulting 10 possible pairing states are summarized in Table I; four states arise from the four one-dimensional (1D) IRs ($d_n = 1$) and three from each of the two 2D IRs ($d_n = 2$). Here we choose the coordinate system such that k_z refers to the c direction, while k_x and k_y are momenta in the ab plane with k_x pointing along one of the twofold rotation axes of D_{3d} perpendicular to the c direction.

To give explicit expressions for the microscopic form of the different order parameters in Table I, we use the pseudospin basis. Although spin is not a good quantum number in the presence of spin-orbit coupling (and several relevant orbitals), we can still define a (\mathbf{k} -space local) pseudospin basis with the same transformation properties as spin if the system has time-reversal and inversion symmetry. As long as different bands do not come close to each other, we can focus on a single band for a given \mathbf{k} point and, hence, restrict the superconducting order parameter $\Delta(\mathbf{k})$ to be a 2×2 matrix in pseudospin space. As usual, we expand this matrix in the (pseudospin) singlet, ψ , and (pseudospin) triplet, with the triplet vector \mathbf{d} , i.e.,

$$\Delta(\mathbf{k}) = [\sigma_0 \psi(\mathbf{k}) + \mathbf{d}(\mathbf{k}) \cdot \boldsymbol{\sigma}] i \sigma_y, \quad (4)$$

where σ_j , $j = x, y, z$, denote Pauli matrices and σ_0 the identity matrix in pseudospin space. Due to the presence of inversion symmetry, all pairing channels in Table I are either pure singlet (gerade IRs) or triplet (ungerade IRs).

From Refs. [21,22], we know that there are two Fermi surfaces enclosing the Γ point. For this reason, we have analyzed the minimal number of nodal points or lines the different pairing states have on a Fermi surface that encloses the

TABLE I. Possible pairing states in PdTe₂ as constrained by the point group D_{3d} . We use X , Y , and Z to represent real-valued continuous functions on the Brillouin zone with the same transformation properties under D_{3d} as k_x , k_y , and k_z . Here a , b , and c are real coefficients that are not fixed by symmetry and follow from microscopic details of the system. The column TRS indicates whether time-reversal symmetry is preserved (y) or broken (n). The last three columns show the form of the order parameter using the pseudospin basis (see main text), the minimal number of nodes on a Fermi surface enclosing the Γ point, and, for the fully gapped states, whether the phase is necessarily topologically trivial or can be topological depending on microscopic details.

IR	Pairing	d_n	TRS	Order parameter $\Delta i\sigma_y$	Minimal number of nodes per FS	Topology
A_{1g}	s wave	1	y	$a + b(X^2 + Y^2) + cZ^2$	0	trivial
A_{2g}	g wave	1	y	$XZ(X^2 - 3Y^2)$	4 nodal lines	
E_g	$e_{g(1,0)}$ wave	2	y	$a(X^2 - Y^2) + bYZ$	2 nodal lines	
E_g	$e_{g(0,1)}$ wave	2	y	$aXY + bXZ$	2 nodal lines	
E_g	$e_{g(1,i)}$ wave	2	n	$a(X + iY)^2 + bZ(Y + iX)$	2 nodal points	
A_{1u}	p wave	1	y	$a(X\sigma_x + Y\sigma_y) + bZ\sigma_z$	0	trivial/top.
A_{2u}	p wave	1	y	$a(Y\sigma_x - X\sigma_y) + bX(X^2 - 3Y^2)\sigma_z$	2 nodal points	
E_u	$e_{u(1,0)}$ wave	2	y	$aX(X^2 - 3Y^2)\sigma_x + bZ\sigma_y + cY\sigma_z$	0	trivial/top.
E_u	$e_{u(0,1)}$ wave	2	y	$aZ\sigma_x + bX(X^2 - 3Y^2)\sigma_y + cX\sigma_z$	2 nodal points	
E_u	$e_{u(1,i)}$ wave	2	n	$[aZ + ibX(X^2 - 3Y^2)](\sigma_x + i\sigma_y) + c(X + iY)\sigma_z$	2 nodal points [44]	

Γ point. From the results summarized in Table I, we can see that 7 out of the 10 pairing states will necessarily give rise to nodal lines or points and are, hence, inconsistent with our penetration depth measurements that indicate a fully established gap on all Fermi surfaces. Consequently, only three pairing states remain possible: the s -wave singlet state, the p -wave order parameter transforming under A_{1u} , and the $e_{u(1,0)}$ state.

Due to the preserved time-reversal symmetry, all of the remaining candidate pairing states belong to symmetry class DIII which is characterized by a \mathbb{Z} topological invariant ν in three spatial dimensions [1]. To analyze ν , let us first focus on one of the bands enclosing the Γ point. In the case of the s -wave singlet state, we just have the standard BCS s -wave superconductor that is known to be topologically trivial. In the limit where the separation between the different bands at the Fermi level is larger than the superconducting order parameter, the invariant ν of the full system is given by the sum of the invariants ν_n of the different Fermi surfaces n , i.e., $\nu = \sum_n \nu_n$ [30]. For the s -wave singlet state, we just have $\nu_n = 0$ on all Fermi surfaces n and, hence, a trivial state $\nu = 0$, irrespective of the relative phases of the order parameter on the different bands.

This is different for the A_{1u} state: Focusing for the moment on the leading terms of the basis functions in the vicinity of the Γ point, $X \sim k_x$, $Y \sim k_y$, and $Z \sim k_z$, the corresponding triplet vector reads $\mathbf{d}(\mathbf{k}) \sim (ak_x, ak_y, bk_z)$. For just a single Fermi surface enclosing the Γ point, we thus have an anisotropic form of the Balian-Werthamer state of the B phase of superfluid ³He. This state is known to be topologically nontrivial with $|\nu| = 1$ [1,46]. Taking into account higher order terms in X, Y, Z , the invariant of the single Fermi surface can be different but must always be odd and, hence, nontrivial. This follows from the general result of Ref. [7] stating that the parity of the invariant ν of a superconducting order parameter that is odd under inversion is given by the parity of the number N_θ of the time-reversal-invariant momenta ($\mathbf{k} = -\mathbf{k}$) enclosed by the Fermi surfaces of the system (which is one in the present case with one Fermi surface around the Γ point), $\nu \bmod 2 = N_\theta \bmod 2$.

Unfortunately, we cannot apply the criterion for topological superconductivity of Ref. [7] to the invariant ν of the full

system as the total number of enclosed time-reversal momenta is even [21,22]. In other words, the interplay between different bands that are topological individually determines whether $\nu = 0$ or $\nu \neq 0$. For example, if there is no additional sign change of the triplet order parameter between the two Fermi surfaces enclosing the Γ point, the invariants of the two bands add to the nontrivial value $\nu = 2$; see Fig. 5(a). On the

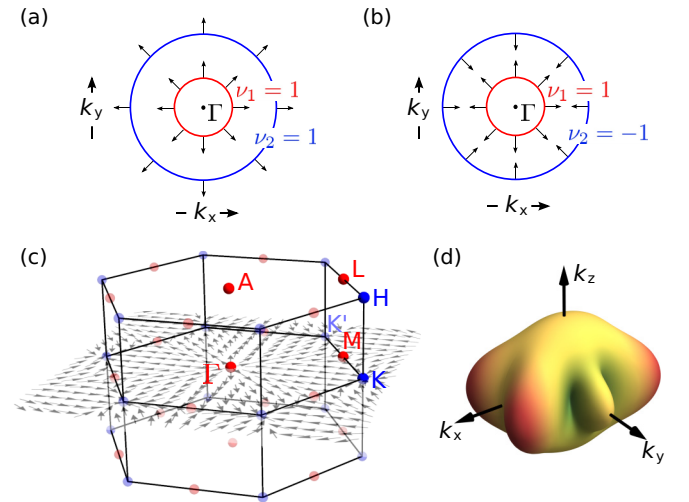


FIG. 5. The triplet vector (black arrows) on the two Fermi surfaces (red and blue solid lines) enclosing the Γ point is shown in (a), for the same sign of the order parameter on the two Fermi surfaces, and (b), for opposite signs, yielding a topologically nontrivial ($\nu_1 + \nu_2 \neq 0$) and trivial state ($\nu_1 + \nu_2 = 0$), respectively. In (c), we indicate the high-symmetry points, where the triplet vectors of the two candidate states, A_{1u} and $e_{u(1,0)}$ in Table I, have to vanish as a consequence of inversion symmetry (red dots) and rotation symmetries (blue dots). The gray arrows illustrate the (simplest) texture of the triplet vector of the A_{1u} state in the $k_z = 0$ plane (with minimal number of defects). Panel (d) shows the directional dependence (i.e., anisotropy) of the gap of the $e_{u(1,0)}$ state on a Fermi surface enclosing the Γ point. The distance of the surface to the origin is proportional to the magnitude of the gap. The state breaks the threefold rotation symmetry and its gap is, thus, generically anisotropic.

other hand, in the presence of an additional sign change, the invariants cancel, resulting in a trivial state, $\nu = 0$, as illustrated in Fig. 5(b). In general, the situation is more complicated due to the presence of additional pockets [21,22] away from the Γ point. For example, the predicted pockets around the K and K' points are generically expected to yield a nontrivial contribution to ν although K, K' are not time-reversal invariant. The reason is that the K and K' points are high-symmetry points where the triplet vector of the A_{1u} state is forced to vanish due to rotational symmetry [see Fig. 5(c)]. Symmetry also enforces that the contributions ν_K and $\nu_{K'}$ of the Fermi surfaces enclosing the K and K' points to the invariant are equal, i.e., $\nu_K = \nu_{K'}$. This can also be seen in Fig. 5(c) upon noting that the z component of the triplet vector of the A_{1u} state transforms as $\sin(k_z)$ under D_{3d} . Consequently, the textures of the triplet vector on, say, spherical Fermi surfaces around the K and K' points are equivalent. This originates in the fact that K transforms into K' under inversion while the triplet vector changes sign under this symmetry transformation.

While both pairing states discussed so far have a gap that is invariant under all symmetry operations of the normal state, the third candidate, the $e_{u(1,0)}$ state, transforms as k_x under D_{3d} and, hence, has a gap that breaks the threefold rotation symmetry along the c axis; see Fig. 5(d). The size of the anisotropy $\propto \Delta_{\min}/\Delta_{\max}$ depends on microscopic details. Given that we observe a full gap behavior in $\Delta\lambda$ for all temperatures, we can exclude a large anisotropy, as for $T > \Delta_{\min}$ one would expect an effectively nodal behavior. While we cannot exclude such fine tuning to a largely isotropic gap state, it makes the pairing candidate $e_{u(1,0)}$ less likely.

The invariant ν of the $e_{u(1,0)}$ state can be deduced by adiabatic deformation from the other triplet candidate A_{1u} : as we show explicitly in the Appendix, choosing the lowest order basis functions, $X \sim k_x$, $Y \sim k_y$, and $Z \sim k_z$, again gives $|\nu| = 1$ for a single Fermi surface enclosing the Γ point. In fact, the previous discussion of the topological invariant of the A_{1u} state based on Ref. [7] equally well applies to the $e_{u(1,0)}$ -wave order parameter.

As indicated in the last column of Table I, this shows that, while the s -wave phase is a topologically trivial state, both of the odd-parity candidate phases can be either topologically trivial or nontrivial depending on microscopic details.

V. CONCLUSIONS AND OUTLOOK

We have presented measurements of the London penetration depth using TDR technique and of the resistivity in single crystals of the type-II Dirac semimetal PdTe₂. Our results reveal that the SC state is fully gapped and characterized by a single-gap energy scale. This is in agreement with previous STM, magnetization, and AC susceptibility results. We determine a zero-temperature London penetration depth of $\lambda(0) \approx 230$ nm from a fit of our measurements of $\Delta\lambda(T)$. Using the previously measured value of the coherence length $\xi = 439$ nm [27], one finds a Ginzburg-Landau parameter $\kappa = \lambda/\xi \approx 0.52$, corresponding to type-I superconductivity, in agreement with previous results [27]. We also report a temperature dependence of the resistivity and its anisotropy that do not reveal any anomalous features and instead closely

follow expectations for an isotropic metal with dominant phonon scattering.

We have performed a systematic theoretical analysis of all possible SC pairing states that can be reached by a single continuous phase transition from the normal state. Using as input our results of a full superconducting gap together with the known form of the Fermi surfaces [21,22], we are able to narrow down the possible SC pairing states to only three candidates: an s -wave superconductor transforming trivially under all symmetries of the lattice, a p -wave phase transforming under A_{1u} , and a triplet order parameter ($e_{u(1,0)}$) transforming as k_x under D_{3d} .

While the first state is always topologically trivial, the latter two triplet phases can be topologically nontrivial, depending on the relative sign of the SC order parameter on different Fermi surfaces. The crucial difference between the triplet states is that the gap of the A_{1u} order parameter is invariant under all lattice symmetries, whereas the gap of the $e_{u(1,0)}$ state breaks the threefold rotation symmetry along the c axis of the normal state.

While our transport measurements indicate the relevance of phonons for momentum relaxation, it is not clear whether phonons also provide the pairing glue. This is important as electron-phonon coupling alone is expected to yield a topologically trivial state, even in the (time-reversal-symmetric) Weyl SM state that can be reached by adding an inversion-symmetry-breaking perturbation [47,48]. The situation is different for magnetic Weyl SMs, which preserve inversion symmetry. Here, the singlet s -wave pairing state is not allowed due to the spin structure around the Weyl points and the pairing state necessarily has odd parity [3]. Alternatively, adding magnetic impurities may, in principle, also result in topological superconductivity [48]. Further microscopic calculations are necessary to understand the connection between the interplay of different electron-electron interaction channels and the resulting superconducting order parameter.

Finally, to experimentally distinguish between the remaining candidate states, we suggest investigating the different behavior of the SC transition temperature and low-temperature behavior of the London penetration depth when tuning the impurity scattering rate, e.g., via electron irradiation as was done, for example, in iron-based superconductors [49].

ACKNOWLEDGMENTS

The authors would like to thank Morgan Masters, Joshua Slagle, and Victor Barrera Escolar for support during the crystal growth. The experimental work was supported by the US Department of Energy (DOE), Office of Basic Energy Sciences, Division of Materials Sciences and Engineering. The experimental research was performed at Ames Laboratory, which is operated for the US DOE by Iowa State University under Contract No. DE-AC02-07CH11358. N.H.J. is supported by the Gordon and Betty Moore Foundation's EPiQS Initiative (Grant No. GBMF4411). M.S.S. acknowledges support from the German National Academy of Sciences Leopoldina

through Grant No. LPDS 2016-12. P.P.O. acknowledges support from Iowa State University Startup Funds.

APPENDIX: ADIABATIC DEFORMATION OF THE $e_{u(1,0)}$ STATE

For completeness, we here present a simple argument showing that the two candidate triplet states, A_{1u} and $e_{u(1,0)}$ in Table I with leading order basis functions around the Γ point ($X \sim k_x$, $Y \sim k_y$, $Z \sim k_z$), are topologically equivalent, i.e., have the same topological invariant ν . To this end, let us define the set of triplet vectors

$$\mathbf{d}_\eta(\mathbf{k}) = (a(1-\eta)k_x(k_x^2 - 3k_y^2) + a\eta k_x, bk_z, ck_y), \quad (\text{A1})$$

which can be used to interpolate between the $e_{u(1,0)}$ state, at $\eta = 0$, and

$$\mathbf{d}_{\eta=1}(\mathbf{k}) = (ak_x, bk_z, ck_y). \quad (\text{A2})$$

It is easily seen that $|\mathbf{d}_\eta(\mathbf{k})| \neq 0$ for $0 \leq \eta \leq 1$, $\mathbf{k} \neq 0$. Consequently, the gap does not close which guarantees that ν does not change during the deformation. Performing a rotation in spin space, which again keeps the gap intact and does not affect ν , the triplet vector in Eq. (A2) can be deformed continuously into $-(ak_x, ck_y, bk_z)$. This is the form of the triplet vector of the A_{1u} order parameter, which proves the topological equivalence of the two states.

-
- [1] X.-L. Qi and S.-C. Zhang, *Rev. Mod. Phys.* **83**, 1057 (2011).
 [2] M. Z. Hasan and C. L. Kane, *Rev. Mod. Phys.* **82**, 3045 (2010).
 [3] M. Sato and Y. Ando, *Rep. Prog. Phys.* **80**, 076501 (2017).
 [4] N. Read and D. Green, *Phys. Rev. B* **61**, 10267 (2000).
 [5] A. Kitaev, *Phys. Usp.* **44**, 131 (2001).
 [6] C. Nayak, S. H. Simon, A. Stern, M. Freedman, and S. D. Sarma, *Rev. Mod. Phys.* **80**, 1083 (2008).
 [7] L. Fu and E. Berg, *Phys. Rev. Lett.* **105**, 097001 (2010).
 [8] Y. S. Hor, A. J. Williams, J. G. Checkelsky, P. Roushan, J. Seo, Q. Xu, H. W. Zandbergen, A. Yazdani, N. P. Ong, and R. J. Cava, *Phys. Rev. Lett.* **104**, 057001 (2010).
 [9] S. Yonezawa, K. Tajiri, S. Nakata, Y. Nagai, Z. Wang, K. Segawa, Y. Ando, and Y. Maeno, *Nat. Phys.* **13**, 123 (2017).
 [10] L. Zhao, H. Deng, I. Korzhovska, M. Begliarbekov, Z. Chen, E. Andrade, E. Rosenthal, A. Pasupathy, V. Oganessian, and L. Krusin-Elbaum, *Nat. Commun.* **6**, 8279 (2015).
 [11] L. Fu and C. L. Kane, *Phys. Rev. Lett.* **100**, 096407 (2008).
 [12] C. W. J. Beenaker, *Annu. Rev. Condens. Matter Phys.* **4**, 113 (2013).
 [13] G. Y. Cho, J. H. Bardarson, Y.-M. Lu, and J. E. Moore, *Phys. Rev. B* **86**, 214514 (2012).
 [14] G. Bednik, A. A. Zyuzin, and A. A. Burkov, *Phys. Rev. B* **92**, 035153 (2015).
 [15] N. P. Armitage, E. J. Mele, and A. Vishwanath, *Rev. Mod. Phys.* **90**, 015001 (2018).
 [16] P. Hosur, X. Dai, Z. Fang, and X.-L. Qi, *Phys. Rev. B* **90**, 045130 (2014).
 [17] L. P. He, Y. T. Jia, S. J. Zhang, X. C. Hong, C. Q. Jin, and S. Y. Li, *NPJ Quantum Mater.* **1**, 16014 (2016).
 [18] Z. K. Liu, B. Zhou, Y. Zhang, Z. J. Wang, H. M. Weng, D. Prabhakaran, S.-K. Mo, Z. X. Shen, Z. Fang, X. Dai, Z. Hussain, and Y. L. Chen, *Science* **343**, 864 (2014).
 [19] H.-J. Noh, J. Jeong, E.-J. Cho, K. Kim, B. I. Min, and B.-G. Park, *Phys. Rev. Lett.* **119**, 016401 (2017).
 [20] S. Kobayashi and M. Sato, *Phys. Rev. Lett.* **115**, 187001 (2015).
 [21] F. Fei, X. Bo, R. Wang, B. Wu, J. Jiang, D. Fu, M. Gao, H. Zheng, Y. Chen, X. Wang, H. Bu, F. Song, X. Wan, B. Wang, and G. Wang, *Phys. Rev. B* **96**, 041201(R) (2017).
 [22] Y. Liu, J. Z. Zhao, L. Yu, C.-T. Lin, A.-J. Liang, C. Hu, Y. Ding, Y. Xu, S.-L. He, L. Zhao, G.-D. Liu, X.-L. Dong, J. Zhang, C.-T. Chen, Z.-Y. Xu, H.-M. Weng, X. Dai, Z. Fang, and X.-J. Zhou, *Chin. Phys. Lett.* **32**, 067303 (2015).
 [23] R. C. Xiao, P. L. Gong, Q. S. Wu, W. J. Lu, M. J. Wei, J. Y. Li, H. Y. Lv, X. Luo, P. Tong, X. B. Zhu, and Y. P. Sun, *Phys. Rev. B* **96**, 075101 (2017).
 [24] Ch. J. Raub, V. B. Compton, T. H. Geballe, B. T. Matthias, J. P. Maita, and G. W. Hull, Jr., *J. Phys. Chem. Solids* **26**, 2051 (1965).
 [25] A. Kjekshus and W. B. Pearson, *Can. J. Phys.* **43**, 438 (1965).
 [26] C. T. Van Degrift, *Rev. Sci. Instrum.* **46**, 599 (1975).
 [27] H. Leng, C. Paulsen, Y. K. Huang, and A. de Visser, *Phys. Rev. B* **96**, 220506(R) (2017).
 [28] S. Das, Amit, A. Sirohi, L. Yadav, S. Gayen, Y. Singh, and G. Sheet, *Phys. Rev. B* **97**, 014523 (2018).
 [29] A. Singh and Y. Singh, *Phys. Rev. B* **97**, 054515 (2018).
 [30] X.-L. Qi, T. L. Hughes, and S.-C. Zhang, *Phys. Rev. B* **81**, 134508 (2010).
 [31] P. C. Canfield, T. Kong, U. S. Kaluarachchi, and N. H. Jo, *Philos. Mag.* **96**, 84 (2016).
 [32] P. C. Canfield and Z. Fisk, *Philos. Mag. B* **65**, 1117 (1992).
 [33] M. A. Tanatar, A. E. Böhmer, E. I. Timmons, M. Schütt, G. Drachuck, V. Taufour, K. Kothapalli, A. Kreyssig, S. L. Bud'ko, P. C. Canfield, R. M. Fernandes, and R. Prozorov, *Phys. Rev. Lett.* **117**, 127001 (2016).
 [34] H. C. Montgomery, *J. Appl. Phys.* **42**, 2971 (1971).
 [35] B. F. Logan, S. O. Rice, and R. F. Wick, *J. Appl. Phys.* **42**, 2975 (1971).
 [36] R. Prozorov, R. W. Giannetta, A. Carrington, and F. M. Araujo-Moreira, *Phys. Rev. B* **62**, 115 (2000).
 [37] R. Prozorov and R. W. Giannetta, *Supercond. Sci. Technol.* **19**, R41 (2006).
 [38] M. A. Tanatar, V. A. Bondarenko, E. I. Timmons, and R. Prozorov, *Rev. Sci. Instrum.* **89**, 013903 (2018).
 [39] K. Kudo, H. Ishii, and M. Nohara, *Phys. Rev. B* **93**, 140505(R) (2016).
 [40] J. P. Jan and H. L. Skriver, *J. Phys. F: Met. Phys.* **7**, 1719 (1977).
 [41] R. Prozorov and V. G. Kogan, *Rep. Progr. Phys.* **74**, 124505 (2011).
 [42] J. R. Schrieffer, *Theory of Superconductivity* (Westview Press, Boulder, CO, 1971).
 [43] A. de Visser (private communication).
 [44] The $e_{u(1,i)}$ state is a special case as it is nonunitary and, hence, leads to two gaps on an initially spin-degenerate Fermi surface

- [45]. While one of the gaps is nonzero, the other one necessarily has nodal points on the k_z axis.
- [45] M. Sigrist and K. Ueda, *Rev. Mod. Phys.* **63**, 239 (1991).
- [46] G. E. Volovik, *The Universe in a Helium Droplet* (Oxford University Press, Oxford, 2003).
- [47] P. M. R. Brydon, S. D. Sarma, H.-Y. Hui, and J. D. Sau, *Phys. Rev. B* **90**, 184512 (2014).
- [48] M. S. Scheurer, *Phys. Rev. B* **93**, 174509 (2016).
- [49] K. Cho, M. Kończykowski, S. Teknowijoyo, M. A. Tanatar, Y. Liu, T. A. Lograsso, W. E. Straszheim, V. Mishra, S. Maiti, P. J. Hirschfeld, and R. Prozorov, *Sci. Adv.* **2**, e1600807 (2016).